

An edited version of this paper was published by [AGU](#).

Origin of volcanism on the flanks of the Pacific-Antarctic ridge between 41°30'S and 52°S

Anne Briaïs^{1,*}, H  l  ne Ondr  as², Frauke Klingelhofer², Laure Dosso³, C  dric Hamelin⁴, Herv   Guillou⁵

¹ LDTP, Observatoire Midi-Pyr  n  es, Universit   de Toulouse, CNRS, 14, Avenue E. Belin, F-31400 Toulouse, France

² IFREMER, B.P.70, F-29280 Plouzan  , France

³ Domaines Oc  aniques, UMR 6538, IFREMER, CNRS, B.P.70, F-29280 Plouzan  , France

⁴ IUEM, UBO, Place Nicolas Copernic, F-29280 Plouzan  , France

⁵ Laboratoire des Sciences du Climat et de l'Environnement, CNRS, B  timent 12, Avenue de la Terrasse, F-91198 Gif sur Yvette, France

*: Corresponding author : A. Bria  s, email address : Anne.Bria  s@ntp.obs-mip.fr

Abstract:

Non-hot spot, intraplate volcanism is a common feature near the East Pacific Rise or Pacific-Antarctic ridge. Volcanic ridges and seamount chains, tens to hundreds of kilometers long, are asymmetrically distributed about the ridge axis, with most volcanic features occurring on the Pacific plate. Their origins remain controversial. We have analyzed off-axis volcanic ridges near the Pacific-Antarctic ridge from bathymetry, backscatter, gravity, and geochemistry data of the Pacantarctic 2 cruise. K/Ar dating of samples dredged on these structures reveals a contrast of up to 3 Ma between the volcanoes and the underlying crust. The volcanic activity, as suggested by the strong backscatter in sonar images, appears to be limited to areas of seafloor younger than about 3 Ma. All surveyed ridges north of the Menard transform fault (TF) show recent activity close to the ridge axis and are not affected by faults. The off-axis volcanic ridges south of the Menard TF show recent volcanic flows in their center and are affected by N-S extension. Two different types of volcanoes can be characterized: conical, flat-topped ones and rough, elongated ones associated with narrow, E-W trending volcanic ridges, some of them showing strong backscattering on the EM12 imagery. From the morphology of the seamount chains and the ages of the lava samples, we infer that the magma source for the volcanic ridges is related to the feeding of the ridge axis through three-dimensional mantle convective circulation. We suggest that a change in the relative plate motion since about 5 Ma might have induced an offset of the mantle upwelling circulation under the ridge axis so that anomalously hot mantle rises under the Pacific ridge flank. The kinematic change is also likely responsible for the tectonic deformation in the young lithosphere south of Menard TF.

Keywords: mid-ocean ridges; off-axis volcanism; mantle convection; plate kinematics; transform fault.

1. Introduction

Off-axis volcanic seamounts and chains away from hotspots have been widely observed in the Pacific, at all scales, close to the ridge axis as well as far from it (e.g., Scheirer and Macdonald, 1995; Smith and Jordan, 1987; Wessel and Lyons, 1997; White, et al., 1998). Many of these volcanoes have been revealed by the gravity maps derived

from satellite altimetry measurements [Sandwell and Smith, 1997; Wessel and Lyons, 1997]. Isolated seamounts mostly form on ocean crust of an age of 0.1 to 1.5 Ma, and appear to be fed by the ridge axial magma supply, sometimes through fractures near axial discontinuity traces (e.g. Gomez and Briais, 2000; White, et al., 2002). Seamount chains and volcanic ridges may form much farther from the East Pacific Rise (EPR) axis and have a magma source distinct from the ridge axial area. The major seamount chains and volcanic ridges in the area between 15 and 20°S have been the focus of recent studies [Forsyth, et al., 2006; Harmon, et al., 2006; Sandwell and Fialko, 2004]. They are associated with troughs of gravity lineaments observed in maps derived from satellite altimetry measurements [Haxby and Weissel, 1986; Sandwell and Fialko, 2004]. Despite numerous studies, the origin of the magma and the mechanism which allows its extraction to form the chains are still debated. Two different kinds of models have been suggested to explain their formation. One type of model involves lithospheric extension or cracking (e.g., Sandwell and Fialko, 2004), while another type implies anomalous melting in the asthenosphere or small-scale mantle convection [Forsyth, et al., 2006; Harmon, et al., 2006; Scheirer, et al., 1996].

During the Pacantarctic 2 cruise of the R/V *L'Atalante* (December 2004), we mapped and dredged several off-axis volcanic edifices which appear as gravity highs on the flanks of the Pacific-Antarctic ridge (PAR) between 40°S and 55°S on the gravity grids derived from satellite altimetry measurements (Figure 1). The investigated structures comprise (Figure 2, Table 1): (a) two ridges near 42°S west of the ridge axis (thereafter referred to as the “42°S ridges”), (b) a relatively short ridge near 47°S, also on the western ridge flank (“Gros Temps” – Bad weather – ridge), and (c) two seamount chains on either side of the Menard transform fault (MTF) near 50°S (“North Menard” and “South Menard” ridges). In each of these regions, bathymetric, magnetic and gravity data were acquired. Dredge samples were retrieved on most large seamounts, except on the “Gros Temps” ridge due to bad weather. The objective of this part of the cruise was to understand how these structures formed, in particular how they relate to axial dynamics and recent kinematics. We present a tectonic and volcanic analysis of the volcanic ridges based on bathymetry, imagery and gravity data. We then compare this analysis to those of other volcanic chains in the central Pacific, and discuss their possible origin.

2. Tectonic setting

The Pacific-Antarctic ridge extends between the Chile triple junction at the Juan Fernandez microplate and the Macquarie triple junction (e.g., Mayes, et al., 1990; Molnar, et al., 1975). Few surveys have been carried out on the southern part of this ridge because of both its remoteness and the sea conditions [Cande, et al., 1995; Lonsdale, 1986; Lonsdale, 1994]. The 1800 km-long section of the southern Pacific-Antarctic ridge extending between 65°30'S and the Udintsev fracture zone (57°S) has been surveyed during the Pacantarctic 1 cruise in 1996 [Géli, et al., 1997; Ondréas, et al., 2001]. That section of the ridge has a half-spreading rate of 27 km/Ma near the Pitman TF and 38 km/Ma near the Udintsev TF. It comprises sections of ridge with an axial valley or an axial high and generally displays a very low cross-sectional relief. Numerous changes in the Pacific-Antarctic plate motion have occurred since 70 Ma [Cande, et al., 1995; Cande and Stock, 2004; Croon, et al., 2008]. The results of the Pacantarctic 1 cruise have shown the importance of these changes on morphological reorganizations of the ridge axis [Briais,

et al., 2002; *Géli, et al.*, 1997; *Ondréas, et al.*, 2001]. They have also emphasized the relationships between heterogeneities in upper mantle temperature, geochemical segmentation of the upper mantle and seafloor morphology.

The northeastern section of the ridge, between the Eltanin transform system and the Juan Fernandez microplate (Figure 1), is a fast-spreading ridge, with half-spreading rates of 41 km/Ma near 52°S and 47 km/Ma near 42°S [*Cande and Stock*, 2004]. It is segmented by the right-stepping Raitt transform fault at 54°30'S, the left-stepping Vacquier transform fault at 53°S and the right-stepping MTF at 49°30'S. The 1600 km-long ridge section between the MTF and the Juan Fernandez microplate shows no transform fault. The Foundation hotspot seamount chain approaches the ridge axis near 37°30'S, forming a complex pattern of volcanic chains [*Maia, et al.*, 2000; *Maia, et al.*, 2001].

During the Pacantarctic 2 cruise, carried out in December 2004 and January 2005, the ridge section between 42°S and 52°S was mapped, and sampled for the first time. This part of the ridge is relatively far from hotspots, located more than 1000 km from the Louisville hotspot to the south, and 400 km away from the Foundation hotspot to the north. The axis direction varies from N10°E to N20°E. This section of the PAR is segmented by the 200 km-long MTF at 49°30'S, and by overlapping spreading centers (OSCs) defining second-order axial segments [*Dosso, et al.*, 2005; *Klingelhoefer, et al.*, 2006; *Lonsdale*, 1994]. *Klingelhoefer et al.* [2006] have analyzed the structure of the ridge axis based on bathymetry, gravity and geochemical data from the Pacantarctic 2 cruise. They show that ridge segments just north and south of the MTF are the most robust, with high cross-sectional area and low mantle Bouguer gravity anomaly. The next segments to the north and south are anomalously deep. The segments to the north show a general deepening of the axis and a decrease of the $(\text{Nb}/\text{Zr})_N$ values, that is an increase in the depleted character of the basalts. The off-axis ridges north and south of the MTF surveyed during the cruise are located near the ends of the robust segments, at places where the axis direction changes (Figure 2). The 42°S ridges are located near a large OSC.

3. Data acquisition and processing

3.1. Structural data

Our analysis is based on multibeam bathymetry and backscatter imagery data, as well as gravity data and sample geochemical analysis and dating from the Pacantarctic 2 cruise. Major off-axis structures were identified on the satellite-derived gravity maps [*Sandwell and Smith*, 1997]. Ship routes during the survey were chosen to maximize the bathymetry coverage and sample collection of these off-axis features as well as a section of axis that was never sampled before. The bathymetric data were acquired using a SIMRAD EM12-dual multibeam system, which comprises two echosounders each with 81 beams, with an overlap of 10 beams under the nadir for data calibration. Sampling period was 20 s, corresponding to about 100 m along track at the ship speed of 10 knots. During the Pacantarctic 2 cruise the aperture angle was chosen to be 140° or 128° depending on the seafloor depths, leading to about 150 m across-track resolution. The swath coverage was 6–7 times the water depth, which corresponds to 15–20 km swath for most of the surveyed area, except near the top of large, shallow volcanoes where the swath narrowed to only a few km. Due to signal processing, imagery has a much higher resolution than the corresponding swath bathymetry. Bathymetry and imagery data have been processed and

mosaicked using the Caribes software. Seafloor backscatter intensity, or reflectivity, is higher on steep slopes such as seamounts slopes or tectonic scarps, on recent lava flows, and possibly on talus and mass wasting occurring over steep volcanic or scarp slopes. Backscatter is low on smooth, sedimented areas. The height of the seamounts above the surrounding seafloor has been calculated relative to a model of lithospheric cooling. For this, we have subtracted the model of seafloor topography predicted by Stein and Stein [1992] from the measured bathymetry, using the crustal ages of Müller *et al.* [1997].

To compare the orientation of volcanic ridges with the relative or absolute plate motions, we estimated flow lines for points from the ridge axis using poles of rotation determined by Cande and Stock [2004]. We used the absolute plate motion from the HS3-NUVEL1a model [Gripp and Gordon, 2002].

3.2. Gravity analysis

Although gravity data were acquired with a Bodenseewerk gravity meter during the complete cruise, the usable gravity measurements only represent small transit lines between seamounts, because the top of the volcanoes was mostly the site of a dredge, at a low speed, leading to noisy gravity data. Therefore we chose to use the satellite-derived gravity anomalies [Sandwell and Smith, 1997; Sandwell and Smith, 2005] for the calculation of the gravity anomalies near the off-axis volcanoes. To test the validity of this choice, we estimated the differences between the ship-borne free-air gravity anomaly (FAA) measurements made during the cruise and the free-air gravity derived from altimetry. Over the entire cruise both types of measurements agree well, with differences of ± 5 mGal. In the Menard area, the differences are relatively large near the top of the volcanoes, and between volcanic ridges in the south, sometimes reaching 15 mGal (Joseph-Louis, unpubl. rep.). We are therefore aware that the absolute values of the gravity anomalies near the seamounts should not be used, and are especially careful in interpreting the anomalies.

Mantle Bouguer gravity anomalies (MBA) were first calculated by subtracting the effect of a constant thickness (6 km), constant density crustal layer from the observed FAA, thereby assuming that the Moho topography paralleled the seafloor bathymetry, using the method of Parker [1972]. The densities for seawater, crust and mantle were assumed to be 1030, 2800 and 3300 kg/m³, respectively. We then removed the effects of lithospheric cooling, using the method described by Ito and Lin [1995], to obtain residual MBA (RMBA). The RMBA map shows large-amplitude negative anomalies, limited to the volcanic ridge areas (Figures 5a, b). To access a more realistic subsurface crustal structure from the interpretation of gravity anomalies, we isolated the seamounts and volcanic constructions from the background topography using an approach similar to that of Shen, *et al.* [1993]. We considered that all reliefs with a bathymetry anomaly higher than 200 m with respect to Stein and Stein [1992] thermal cooling model were volcanic constructions. We removed these highs and replaced them with the “normal” bathymetry predicted by the cooling model. We then filtered the remaining topography using a median filter of 20 km radius. We estimated MBA using this more realistic model, with a crustal layer having the smooth bathymetry estimated above, and the effect of a “volcanic” layer limited by the measured bathymetry (with a density of 2300 kg/m³). The resulting RMBA (Figures 5c, d) have a lower amplitude compared to those estimated using the real bathymetry.

The pattern of intermediate-wavelength gravity lineaments in the Central Pacific has

lead Haxby and Weissel [1986] to interpret them as evidence for small-scale mantle convection in the asthenosphere under the oceanic lithosphere [Haxby and Weissel, 1986]. A major observation was that some lineations are oblique to the fracture zones but sub-parallel to the absolute plate motion. From improved gravity grids, Sandwell and Fialko [2004] confirm the oblique orientation of lineations with respect to spreading direction, and show that the major volcanic ridges in the Central Pacific are preferentially observed in the troughs of the gravity lineaments. The authors suggest that the lineaments and the cracks above which volcanic ridges form result from thermoelastic stresses in the cooling lithosphere.

We have filtered the satellite-derived free-air gravity anomalies [Sandwell and Smith, 2005] to enhance possible gravity lineations as observed in the Central Pacific. The gravity field of the small-scale features was removed using a two-step low-pass filter (median filter, then low-pass 80 km filter). The resulting field was then high-pass filtered to remove wavelengths longer than 600 km.

3.3. Geochemical analysis

Samples have been collected on the summit of the major off-axis volcanoes: four dredges from the 42°S ridges, four dredges from the ridge north of the Menard TF, and nine dredges from the ridge south of it (Figure 3, Table 2). All samples were crushed to centimeter size fragments. Pieces of glass or chips from the inner part of lava flows or pillow lavas were handpicked to avoid altered surfaces. All samples (either glasses or rock chips) were washed in an ultrasonic bath of 2M HCl, followed by double distilled water before further crushing in an agate mortar for trace element analysis. Trace element analyses were performed by ICP-MS at Brest using Finnigan Element2 and following the method described in Barrat, *et al.* [1996] and Etoubleau, *et al.* [1999]. Based on standard measurements and sample duplicates trace element concentrations reproducibility is generally better than 5% [Barrat, *et al.*, 2007].

3.4. K-Ar dating

Nine samples were selected for K-Ar dating, based on the geological setting of the dredge site and the results of the geochemical analysis (Figure 3, Table 3). Only rocks without traces of alteration were selected, and prepared following the method described in Guillou, *et al.* [1996]. Glassy samples were avoided because of possible excess argon caused by rapid quenching which could prevent loss of non-atmospheric initial argon.

The samples were crushed and sieved to 0.250–0.125 mm size fractions and ultrasonically washed in acetic acid, to remove secondary mineral phases that might be present in minute amounts. Phenocrysts and xenocrysts which may carry excess ^{40}Ar were removed using heavy liquids of appropriate densities and magnetic separations. K and Ar measurements were performed on the groundmass fractions of each sample. Potassium was analyzed by atomic absorption with a relative precision of 1%. The instrument and unspiked technique used to determine the isotopic composition of Ar and the Ar content are those presented and discussed in details in Cassagnol, *et al.* [1978], Charbit, *et al.* [1998], and Gillot and Cornette [1986].

This technique dynamically compares the isotopic composition of an aliquot of pure atmospheric Ar with the sample Ar and allows accurate determination of minor variations of the $^{40}\text{Ar}/^{36}\text{Ar}$ isotopic ratios between the standard and the unknown. Therefore, very

small amounts (<1%) of $^{40}\text{Ar}^*$ can be detected and accurately quantified and this technique can be successfully applied to date Quaternary submarine volcanic rocks [Ravilly, *et al.*, 2001; Vlastelic, *et al.*, 1998]. Argon was extracted from 1 to 2 g of sample by radiofrequency heating induction in a high vacuum glass line, and purified with titanium sponge and Zr–Al getters. Isotopic analyses were made on Ar quantities ranging from $1.0 \cdot 10^{-11}$ to $3.8 \cdot 10^{-11}$ moles, using a 180° , 6 cm radius mass spectrometer operated at an accelerating potential of 620 volts. The spectrometer was operated in a semi-static mode. Data were collected on a double faraday collector in sets of 100 using a 1 s integration time. The sensitivity of the mass spectrometer is about $5.1 \cdot 10^{-15}$ moles/mV with an amplifier background of 0.075 V for ^{40}Ar and 5.75 mV for ^{36}Ar . Procedural blanks were measured between $5 \cdot 10^{-12}$ and $1.2 \cdot 10^{-11}$ moles with an atmospheric isotopic composition. This technique is not suitable to check if the initial $^{40}\text{Ar}/^{36}\text{Ar}$ ratio has a value equivalent to the modern atmospheric value. Consequently, errors given in Table 3, which are analytical, may be underestimated.

4. Characteristics of volcanic ridges and seamounts

4.1. The 42°S ridges

Three large ridges are located near the large $41^\circ30'\text{S}$ OSC on the satellite gravity map (Figures 1–4, Table 1). They are 150–200 km-long, and spaced about 50 km. At 50 to 100 km distance from the axis, corresponding to a crustal age of 2 to 5 Ma (all crustal ages from Müller, *et al.* [1997]), the ridges terminate and appear to be offset 30 km to the north, where three shorter ridges are observed, at the same spacing. We mapped the northern large ridge entirely, and the southern recent ridge (Figure 2). The volcanic constructions show a large variation of morphologies (Figures 3a, b). The northern ridge near $41^\circ15'\text{S}$ is 150 km long, 5 to 10 km wide, and rises up to 1500 m above the seafloor. The 70 km-long western section between 114°W and 113°W is a narrow, elongated ridge trending N95E located on seafloor about 4 to 5 Ma. Farther east between $112^\circ40'\text{W}$ and 112°W , it turns into groups of conical, flat-topped seamounts aligned in the E-W direction, all showing calderas. These seamounts are 5 to 10 km in diameter and up to 1500 m above the surrounding seafloor. Around 113°W , between the western ridge and the group of seamounts, the ridge is broader and displays some N80E-trending scarps. The backscatter imagery reveals that this northern ridge is surrounded by many small edifices which completely mask abyssal hills. The backscatter intensity tends to decrease with the distance to the axis, suggesting an increase in the sediment thickness and therefore an increase in age.

The ridge extending between $111^\circ40'\text{W}$ and $112^\circ30'\text{W}$ near $41^\circ55'\text{S}$ is very linear, 50 km long, about 7 km wide and culminates at 1500 m above the seafloor. It displays very high backscatter on most of its length. It does not seem to have been formed by the coalescence of individual volcanoes. A lower ridge trending N80°E extends to the east, to about 15 km from the ridge axis. Near $41^\circ35'\text{S}$, we observe several small volcanic mounds and two small volcanoes with calderas. The very dark backscatter image just northwest of this group of volcanoes suggests the presence of recent lava flows.

The RMBA map (Figure 5a,c) shows linear gravity lows underlying the volcanic ridges. The amplitudes of the anomalies are relatively small, suggesting that the seamounts and volcanic ridges are associated neither with a significant crustal root, nor with an

anomalously hot mantle. Such features would produce density anomalies which are not reflected in the observed gravity anomalies.

Two dredges sampled altered pillows from the west of the northern ridge and vesicular basalts from the east. A sample collected at 113°35'W was dated 2.16 ± 0.06 Ma. This age is about 3 Ma younger than the age of the underlying seafloor. Fresh pillows including basaltic glass have been dredged near the center of the southern ridge. A sample was dated 0.46 ± 0.06 Ma, for an underlying crust aged 1 to 2 Ma. All samples show very low $(\text{Nb}/\text{Zr})_N$ values which have rarely been observed along mid-ocean ridges (Table 2). At the same latitude, the axial samples also show relatively low values of $(\text{Nb}/\text{Zr})_N$ compared to axial samples collected farther south [Klingelhofer, *et al.*, 2006]. Gravity and geochemical analyses suggest that these basalts result from depleted mantle with melting rates similar to those at the ridge axis.

The 42°S ridges are located in a gravity low, oblique to the spreading direction, observed in the gravity anomaly maps (Figures 1 and 6). No other clear gravity lineation is observed in this area. This low corresponds to the trace of a large propagator currently located at the axis near 41°30'S. In fact, the satellite-derived gravity map (Figure 1) shows that traces of two propagators join in this area, a northern one propagating south and a southern one propagating north. The present-day OSC is right-stepping and appears to be propagating north. It is likely that the lithosphere in the discontinuity trace is more permeable to magma [White, *et al.*, 2002], as this area undergoes fracturation near the tip of ridge segments [Kleinrock and Hey, 1989], explaining the location of the seamount chains.

These observations show that the 42°S ridges vary in morphology from narrow, straight, elongated ridges clearly resulting from fissure volcanism, to conical volcanoes reflecting point-source volcanism (Figure 3a, b). The narrow ridge forming the western section of the 41°15'S ridge is surrounded by low-relief volcanoes revealed by the backscatter images, suggesting that it did not form only through fissures controlled by tectonic deformation of the lithosphere. The volcanism appears to have localized after an initial volcanism spread across a 15 km-wide zone. To the contrary, the ridge on younger seafloor is clearly controlled by fissure volcanism. Between these ridges, volcanoes are surrounded by numerous small mounds, implying little control by fissures. Since several parallel ridges formed, it is possible that one of them appeared first, and that the others developed at the bulge of the resulting flexure [Hieronymus and Bercovici, 2000]. We do not have enough age information from the limited surveyed and sampled ridges to test this hypothesis and infer which of the ridges was constructed first.

4.2. The Gros Temps ridge

The "Gros Temps" ridge consists in a series of large coalescent volcanoes, 4 to 10 km in diameter, up to 1900 m high (Figures 3c, d). The ridge starts 15 km from the axis, is 50 km long and extends to 2 Ma-old seafloor. The volcanoes of the western, older part of the ridge are aligned in a N75°E direction, oblique with respect to the Pacific relative or absolute plate motion. The more recent section of the chain is aligned closer to the spreading direction, but the northernmost, youngest volcano is aligned with the old ones. Rare tectonic scarps are oriented parallel to the axis or to the volcanic ridge. All volcanoes show calderas, which are sometimes complex and imbricated. Only the northernmost, youngest volcano shows strong backscattering suggesting recent volcanic activity. The

RMBA low associated to the seamount ridge is linear, and has a relatively low amplitude (Figure 5b, d), implying that the ridge does not correspond to a large crustal thickness anomaly.

The oblique arrangement of the volcanic chain suggests that the source of the volcanoes migrates to the north with respect to the plate. The tallest volcano in the chain is the central one, located on 1 Ma-old crust (Figure 4). The Gros Temps chain displays its tallest volcanoes on young seafloor (< 1Ma) among all the surveyed volcanic chains (Figure 4). This suggests that the volcanoes grow faster along this chain than along the other volcanic ridges, implying the availability of a larger amount of magma.

4.3. The North Menard ridge

The North Menard volcanic ridge (Figures 3e, f) is located about 10 km from the axis, and extends 200 km off axis to crust aged 5 Ma. The seamounts surveyed on crust older than 4 Ma are small, deep, sedimented structures. The younger ridge, between 115°40'W and 113°40'W, is formed by large volcanoes connected by thin volcanic ridges. The volcano line is split into several groups. Some ridges extending from the volcano groups or linking them are aligned slightly oblique with respect to Pacific plate motion, such as near 114°30'W and 115°30'W, while most volcano alignments are parallel to the flow lines, like near 115°15'W and 114°15'W. Near 114°45'W, two parallel alignments coexist for the same crustal age, one with a tall volcano adjacent to a narrow volcanic ridge, the other consisting of several deeper, coalescent volcanoes with calderas. The volcanoes have an average diameter of 6 km and are 1000 to 1900 m high. Only the volcano closest to the axis shows strong backscattering suggestive of recent volcanic activity. Recent lava flows are also inferred from the highly reflective areas to its east. All volcanoes are characterized by simple or double calderas open toward the ridge axis. The backscatter image also reveals some small, sedimented, cratered mounds surrounding the main ridge. These small volcanoes appear to be less developed than near the 41°15'S ridge. Toward the southwest end of the map, the N15-N20E fabric of the abyssal hills dominates the seafloor fabric, parallel to the axis. Four dredges on these volcanoes brought back altered basalts, various pillows and some biological samples (corals, galatheas, mussels), respectively from west to east. The few tectonic scarps existing in this region trend EW to N100°E.

K/Ar dating yield ages of 1.21 ± 0.12 Ma for a sample collected on the large volcano at 115°15'W, and 0.152 ± 0.006 Ma for the volcano closest to the ridge axis. The high backscatter suggests that the latter volcano is still growing. The other dated sample belongs to a volcano lying on 3–4 Ma-old crust, leading to an age difference of about 2.5 Ma between the top of the volcano and the underlying crust. The dating and the imagery data therefore suggest an age progression with the distance to the axis.

The RMBA anomalies associated to this volcanic ridge are round and isolated, exhibiting no link between the volcanoes, suggesting that the volcanoes do not feed from a large hot mantle source under the ridge (Figure 5). The 80–600 km-wavelength filtered gravity anomaly map, similar to the map estimated by Haxby and Weissel (1986), displays prominent lineations only in the area of the Menard fracture zone, with 200 km wavelength and up to 20 mGal in amplitude, parallel to the plate motion (relative or absolute) (Figure 6). The gravity undulations have a limited extent compared to the lineations observed in the Central Pacific [Haxby and Weissel, 1986]. The off-axis volcanic ridges on the flanks

of the Pacific-Antarctic ridge appear to be preferentially located in the troughs of the gravity undulations, including in the lows corresponding to large propagators.

The gradual decrease in backscatter energy suggests that the volcanoes in this chain were emplaced close to the axis, and drifted away with the Pacific plate (Figure 3f). This drifting of the volcano with respect to the magma source is also suggested by the opening of the calderas to the east toward the next volcano in line. The tallest volcano in the line is located on crust 2–3 Ma old (Figure 4). It is therefore likely that the volcanoes form near the axis, and grow for about 2 to 3 Ma before they become extinct. The North Menard ridge consists of several sets of volcano groups, suggesting that magma is not available in steady-state flux beneath the ridge, or that distinct episodes of lithospheric deformation allowed for the emplacement of the volcano groups (Figure 3e, f). The gaps between different groups along the chain might result from periods during which less magma was available or lower stresses in the lithosphere did not favor its extraction to the surface. The highest volcanoes of the different groups are separated by about 1 Ma. The high backscatter on the slopes of some of the older volcanoes may result from mass wasting. The North Menard chain is located both near the end of a very robust axial segment and near the trace of the large 48°40'S OSC, two factors which might be favorable to the emplacement of off-axis volcanoes (Figure 2).

4.4. The South Menard ridges

The off-axis volcanic structures south of the Menard TF are the most complex in the study area (Figures 3g, h). These volcanic ridges are the only major volcanic ridges located on the eastern flank of the Pacific-Antarctic ridge (Figure 1). The volcanoes are 12 km in diameter on average, and 1500 to 2000 m above the surrounding seafloor, generally larger than those forming the ridges north of the MTF. The volcanoes are aligned in two ridges, a long, northern one near 50°10'S extending to 5 Ma-old seafloor, and a shorter one near 50°30'S extending only to crust aged a little over 3 Ma. Both ridges trend nearly E-W. They are linked near 115°W by a flat saddle in between two volcanoes.

The volcanic structures display two main types of morphologies. The first type consists of typical conical-shaped or flat-topped volcanoes, with a summit caldera. The flat tops of these structures are characterized by relatively low backscattering in the EM12 imagery data, probably due to the presence of sediments. Such volcanoes are located on lithosphere older than 3 Ma, as well as on younger crust of about 1 Ma age. Dredges near the top of this type of volcanoes recovered altered and porphyric basalts, as well as coarse-grained rocks. The second type of morphology consists of rough topography, highly structured and deformed volcanoes, elongated in the E-W or N70E directions. They are located on crust aged 1 to 3 Ma. They are surrounded, and connected by narrow, EW-trending volcanic ridges. Some of these volcanoes show strong backscattering on the EM12 imagery suggestive of relatively fresh volcanic flows. Plagioclase-bearing pillows as well as aphyric fresh and altered pillows have been dredged near their tops. The volcano at 50°10'S, 116°W (DR16) shows the highest backscatter and the roughest topography. Strong backscatter occurs just north of it, which we interpret to be a relatively fresh lava flows. The ridge-parallel, seafloor fabric is observed around the volcanoes up to crustal ages of about 2 Ma. Near 115°15'W, the large volcanoes in the center of the ridge system appear to have a complex history. The volcano at 50°20'S, 115°15'W (DR14), in the southern ridge, shows multiple cones, partly overlapping, with large calderas. It is

elongated to the northwest and connects with a tall volcano in the north ridge (DR15). The other two volcanoes from the southern volcanic ridge are among the tallest of the whole group, reaching 1800 to 2050 m above seafloor. The morphology and backscatter image suggest that both ridges may be still active near 116°W. The RMBA anomalies show isolated lows, with no link between the volcanoes, except for DR14 and DR15 volcanoes. The DR15 and DR16 volcanoes show higher amplitude gravity anomalies than the other volcanoes, while DR14, DR17 and DR19 volcanoes exhibit less pronounced anomalies. The relative amplitudes and the patterns of the anomalies are similar to the ones estimated in the GLIMPSE study area in the Central Pacific [Harmon, *et al.*, 2006].

Volcanoes located in the center of the seamount chains show fractures and ridges of tectonic origin. Numerous tectonic scarps are observed, implying significant deformation of the lithosphere during or after their emplacement. Scarp orientations are mostly E-W, in the same direction as most small volcanic ridges. The volcano near 50°10'S, 115°15'W (DR17) is cut by two EW synthetic normal faults forming a small graben about 6 km wide. The distribution of the earthquake epicenters south of the MTF also suggests that both seamount chains are affected by tectonic deformation (Figure 1). The focal mechanisms (inset, Figure 1) reveal mostly strike-slip earthquakes, likely to have occurred on the Menard transform fault, but also a few normal fault earthquakes, likely related to extension in the off-axis volcanic area.

The ages determined for the northern volcanic ridge show a progression from 0.4 Ma close to the ridge to 2 Ma (Figure 3h). Unfortunately, no sample from the large DR16 volcano could be dated, because of the size of the dredged rocks. The strong backscatter suggests that it is the most active volcano in the line. In the southern ridge, one volcano lying on 2.5 Ma crust was dated 0.704±0.02 Ma. This volcano is located at the same distance from the axis as the volcano dated 1.04±0.03 Ma on the northern line. This age difference and the difference in length of the ridges suggest that the southern volcanic ridge began to form later than the northern one.

The seamounts are located near the southern end of the robust axial segment south of the transform, close to the major 51°S discontinuity. The northern ridge is located at the latitude of a robust section of ridge axis, showing a maximum in the cross-sectional axial area [Klingelhofer, *et al.*, 2006]. The southern ridge is connected to the southern tip of the segment, close to the discontinuity between the axial segments. The volcanoes generally show low values of (Nb/Zr)_N, typical of depleted basalts (Table 2). The two volcanoes in the southern volcanic ridge (DR12 and DR13), like the volcano in the North Menard ridge that is closest to the ridge axis, show higher values of (Nb/Zr)_N, suggestive of more enriched basalts. The volcanoes displaying these high values are close to axial samples also showing abnormally high values of (Nb/Zr)_N [Klingelhofer, *et al.*, 2006], suggesting a link between magma sources for the off and on-axis volcanism.

The conical morphology of some of the volcanoes in the South Menard ridges suggests that the volcanoes of the northern line, and the DR14 volcano farther south, were not emplaced by fissural volcanism. The general increase in the age difference between the dated samples from the volcanoes and the underlying crust (Figures 3g, h) suggests that they were more likely emplaced near the ridge axis and drifted away from the axis with the Antarctic plate. The most recent activity, however, appears to be controlled by tectonic extension, as evidenced by EW or N45E-trending thin volcanic ridges linking the volcanoes and extending toward the axis, or by normal fault scarps. The volcanoes from

the southern line, and the DR16 volcano of the northern line, have a rough morphology dominated by linear volcanic aprons. They show a higher backscatter signal on the imagery data, suggesting they were built more recently than most of the northern line.

A likely scenario for the history of the South Menard volcanic area is that the northern line was constructed first, with mostly isolated volcanoes emplaced relatively close to the axis. Then the southern line built on the flexural bulge created by the northern line, or as a result of an extensional event. The northern line displays evidence for NS extension, with fissures and faults. The higher $(\text{Nb}/\text{Zr})_N$ ratios observed on the samples from the southern line compared to the northern one suggest that the northern and the southern volcanoes are tapping two distinct magma sources, or that the volcanoes of the two lines originate from different melting processes. Another observation supporting the proposed scenario is that the volume of the volcanoes in the southern line is generally larger than in the northern line, suggesting that the volcanoes grew on thicker lithosphere (Figure 4) [Vogt, 1974]. The age difference for the seafloor beneath the volcanoes is of the order of 1 Ma, except for the central part where the two lines are parallel, which shows age differences of only 0.5 Ma for crust beneath the volcanoes. The observation of a higher $(\text{Nb}/\text{Zr})_N$ ratio for the southern volcanoes in the south Menard system is similar to that at the Foundation seamount chains [Maia, et al., 2001]. The ratio is higher for the volcanoes of the Foundation southern line compared to the northern line. The morphologies are also similar, although the south Menard volcanoes are smaller than the Foundation seamounts. The Foundation volcanoes on the northern line are conical seamounts, while the Foundation seamounts of the southern line are elongated and connected by small ridges, suggesting fissure volcanism partly controlled by tectonic deformation of the lithosphere. Maia et al. (2001) suggest that the southern line is emplaced through the extensional deformation at the bulge of the flexure created by the load of the northern line. It is possible that such a mechanism is also responsible for the formation of the volcanoes south of MTF.

The specific arrangement of the reliefs on either side of the Menard transform fault could be interpreted as reflecting the incipient formation of a microplate. Indeed, the volcanoes furthest from the axis are closest to the transform fault, “closing” a hypothetical microplate. Testing this hypothesis was one of the cruise objectives. Well-studied microplates such as the Easter or the Juan Fernandez microplates are characterized by the overlap of two accretionary ridges, and by zones of compressive deformation between the ridges [Rusby and Searle, 1995; Searle, et al., 2006; Yelles-Chaouche, et al., 1987]. Our observations do not support the microplate hypothesis for several reasons. First, bathymetry and imagery show that the tectonic deformation in the area is accommodated along the ridge axes, the transform fault itself, and the south Menard ridges. The older ends of the volcanic ridges do not show any sign of tectonic deformation in the bathymetry or imagery data. The Menard transform zone is narrow and deep, as expected for active oceanic shear zones. Second, the distribution of the focal mechanisms (Figure 1) mostly just south of the transform fault suggests that the deformation is located only in the transform and along the southern volcanic chain, and not along the northern border of a microplate that would be forming along the north Menard ridge. Admittedly, the location of the earthquake epicenters is uncertain due to the remoteness of the area from seismological stations, but the errors on the locations are not likely to exceed 50 km. Nor is there any reason for the errors to imply a grouping of the earthquake locations south of the

transform if they were originally distributed on both volcanic ridges. Focal mechanisms show mostly strike-slip motion, and a few mechanisms show normal fault mechanisms (Harvard CMT), confirming that the Menard transform fault is still accommodating most of the shear related to the offset of the plate boundary. In the following text other possible mechanisms for the formation of the seamount chains will be discussed.

5. Discussion

Off-axis volcanic ridges and seamount chains have been extensively observed and studied on the Pacific plate, both near the EPR, and away from the axis. The development of seamounts requires a source in the mantle producing enough magma to reach the surface without freezing entirely on the way up, and a mechanism to extract the magma toward the surface through the young lithosphere. The seamount chains we surveyed develop on seafloor younger than 10 Ma, and get as close as 20 or 15 km from the PAR axis, that is 0.3 to 0.4 Ma-old crust. These seamount chains are very similar in size and shape to ridges in the Rano Rahi seamount field, or to the Thanksgiving ridge farther off-axis in the same area (Table 1) [Forsyth, *et al.*, 2006; Lynch, 1999; Scheirer and Macdonald, 1995; Scheirer, *et al.*, 1996]. They are, however, much smaller than the Sojourn or Puka Puka ridges, and extend much closer to the axis than these major ridges. We briefly present various models considered for the production of magma under the ridge flanks and its extraction to the seafloor, and compare the implications of these models with our observations.

5.1. Where does the magma come from?

Several sources of mantle melt, which are not mutually exclusive, have been considered for the feeding of the near-axis volcanic ridges and seamount chains: (i) The magma could come from the ridge axial area. Recent seismic studies show that mantle upwelling beneath the ridge axis is not limited to a narrow zone beneath the axis, but may extend to an area several tens of kilometers wide, not only in the central Pacific anomalous area close to the Rano Rahi seamount field [MELT Seismic Team, 1998; Conder, *et al.*, 2002], but also near the northern EPR [Toomey, *et al.*, 2007]. (ii) Melt could originate from local, thermal or compositional anomalies in the mantle beneath the volcanoes or beneath the ridge axis [Davis and Karsten, 1986; Wilson, 1992]. Such local anomalies have been considered to be partly at the origin of the Rano Rahi seamount field near the EPR [Scheirer, *et al.*, 1996; Shen, *et al.*, 1995]. (iii) Mantle upwelling and melting could result from ridge-perpendicular, small-scale mantle convection beneath the Pacific plate [Haxby and Weissel, 1986]. A model derived from the latter suggests that a small-scale fingering convective pattern in the large-scale mantle return flow from the Pacific superswell to the EPR or PAR axis [Phipps Morgan, *et al.*, 1995] could be responsible for both the gravity lineaments and the emplacement of the long volcanic ridges developing relatively far from the ridge axis in the Central Pacific [Forsyth, *et al.*, 2006; Harmon, *et al.*, 2006; Weeraratne, *et al.*, 2007].

It is difficult to relate the volcanic ridges in our survey area with possible small-scale mantle convection beneath the Pacific plate. One reason is that such convective pattern, resulting from the cooling of the plate, does not develop under lithosphere younger than about 60 Ma [Dumoulin, *et al.*, 2005; van Hunen and Zhong, 2006], much older than the age of the crust under the near-axis seamounts. Another reason is that the off-axis

seamounts are not systematically related to intermediate-wavelength gravity lineaments. The lineaments which appear in the 80–600 km wavelength filtered gravity grid (Figure 6) are limited to the Menard fracture zone area. The limited extension of the gravity lineaments and their orientation parallel to MTF, already noted by Haxby and Weissel [1986], suggest that they may result from crustal processes related to the ridge segmentation. It is interesting to observe that gravity lineaments north of Menard fracture zone actually disappear at crustal ages younger than about 10 Ma (Figure 6). This is the time when the relative plate motion between the Pacific and Antarctic plates accelerated from a full spreading rate of 70 km/Ma to 82 km/Ma [Cande and Stock, 2004]. It is possible that the gravity lineaments near Menard fracture zone reflect crustal thickness variations resulting from axial magmatic segmentation. An increase in the ridge spreading rate may favor the redistribution of crust along the axis and decrease the gravity signature of the segmentation [Bell and Buck, 1992].

Three characteristics of the off-axis volcanoes located on the Pacific plate support the hypothesis in which their source of magma is the partially molten mantle beneath the ridge axis. First, the growth of the volcanoes mostly occurs between 15 and 50 km from the ridge axis. The Gros Temps volcanic chain is even closer to the axis than the other ridges. Second, the backscatter images show that the volcano closest to the axis displays the most recent lava flows. Evidence for recent lava flows in the center of the ridges is only observed in the south Menard volcanic area. Third, the trace element concentrations of the off-axis lavas are most often similar to those of the samples collected along the ridge axis at the same latitude. The trace element concentrations (only Nb and Zr concentrations are presented here) measured in samples collected at the top of off-axis volcanoes show a large diversity. Most samples present low values of $(\text{Nb}/\text{Zr})_{\text{N}}$, typical of depleted basalts (Table 2), similar to the values measured on axial samples [Klingelhofer, et al., 2006]. Some samples show very low values, in particular in the 42°S ridges, and some display high values suggestive of enriched basalts, and in most cases these characteristics are found also on nearby axial samples. These observations suggest that the magma source for the seamounts is very close, or combined to the axial magma source.

The seismic and geophysical investigations along the EPR all concur to the occurrence of partial melting in a broad zone under the ridge axis [MELT Seismic Team, 1998; Toomey, et al., 2007]. The PAR in our survey area has an opening rate similar to that of the northern EPR (80–90 mm/yr), and is about as far from the Pacific superswell (2000–3000 km), which makes it comparable to that ridge section in terms of expected mantle temperature. The seismic tomography image of the northern EPR revealed that mantle upwelling under the ridge axis, inferred from a 20–30 km-wide mantle low-velocity zone, is highly three-dimensional, and that it may be skewed up to 20 km with respect to the plate boundary [Toomey, et al., 2007]. It is therefore likely that, under the northern PAR, the partially molten mantle that provides the ridge axis with magma may be tapped by volcanoes 15 to 50 km off-axis. Because most of the off-axis seamounts of our study occur on the Pacific plate, it is possible that the mantle upwelling feeding the Pacific-Antarctic ridge axis is also offset to the west.

The south Menard and the north Menard volcanic ridges coincide with magma-poor segments S2 and N2 near large-offset axial discontinuities [Klingelhofer, et al., 2006]. It is possible that part of the melt produced under the ridge axis is derived under the flanks of the ridge to build off-axis volcanoes, or that the partially molten mantle is offset to the

west in this area.

The Menard area appears to coincide with a zone of anomalous melting. The axial segments just north and south of the transform are especially robust, as shown by their shallow depth and high cross-sectional area [Klingelhoefer, *et al.*, 2006; Lonsdale, 1994]. It is likely that the axial mantle upwelling is disrupted, or skewed, near the transform. Three-dimensional numerical modelling of mantle flow beneath a ridge-transform-ridge plate boundary suggests that mantle circulation is disrupted in the vicinity of the transform and that the upwellings might be offset with respect to the ridge axis [Rabinowicz, *et al.*, 1993].

A northward migration of the magma sources with respect to the Pacific plate is suggested by our observation of the frequent obliquity of the ridges with respect to plate motion. A variation in time of the location of upwelling is inherent to 3-D mantle circulation, as numerous factors such as the amount of partial melt or water, the temperature, and the interaction with relative or absolute plate motion, and with large-scale mantle flow related to hotspots, all influence the mantle flow patterns (e.g., Kincaid, *et al.*, 1996; Rabinowicz and Briais, 2002).

5.2. How is the magma extracted to form the seamounts?

Lithospheric extensional stresses favoring the extraction of magma to the surface might result from: (i) cracking resulting from the thermal contraction of the cooling mantle [Gans, *et al.*, 2003; Sandwell and Fialko, 2004], (ii) the Pacific plate recent kinematic changes and associated distributed stresses in the plate [Wessel and Kroenke, 2007], or (iii) local membrane stresses resulting from the load of one volcano [Hieronymus and Bercovici, 1999; Hieronymus and Bercovici, 2000].

Lithospheric tensile stresses accommodating the adjustment of the Pacific plate to kinematic changes near 5 Ma might be responsible for the emplacement of the volcanic ridges, especially the south Menard area. All the volcanic constructions we studied are built on seafloor aged 5 Ma or younger (Figures 1, 2, 3), as suggested by the lack of a well-developed anomaly in the satellite-derived gravity anomaly map. The longest ridges, at 42°S, and north and south of the MTF, extend to seafloor aged about 5 Ma. The mechanism responsible for the development of the off-axis volcanic ridges in this area is therefore likely to have been initiated or enhanced at that time, or to affect preferentially the young lithosphere. The observation of linear ridges in all but the Gros Temps seamount chains suggests that the extraction of the magma involves some kind of fissure and axis-parallel extensional stresses. In a detailed reconstruction of the evolution of the Menard transform, Croon *et al.* [2008] reveal that a 3° clockwise change in the Pacific-Antarctic spreading direction occurred since chron C3o (5.1 Ma). The adjustment of the Pacific ridges to the changing spreading direction might have increased the component of ridge parallel tensile stresses since about 5 Ma, favoring the cracking of the young lithosphere and the emplacement of seamounts. In the southern Pacific, a change in the relative Pacific-Antarctic plate motion at that time is responsible for extension in the right-stepping transform faults [Géli, *et al.*, 1997; Ondréas, *et al.*, 2001], as well as for the development of a large-offset propagator along the Pacific-Antarctic ridge [Briais, *et al.*, 2002]. The changes in plate motion might also have induced an offset between the zones of mantle upwelling and the plate boundary, explaining why more off-axis seamounts are observed on the Pacific plate than on the Antarctic one.

A clockwise rotation of the spreading direction results in an extensional component of the right-stepping axial discontinuities, such as the Menard transform fault [Croon, *et al.*, 2008]. It may be possible that the extension observed in the south Menard area is due to this mechanism. Transform faults, however, usually accommodate the extension resulting from kinematic changes by developing intra-transform basins or spreading segments [Pockalny, *et al.*, 1997; Searle, 1983]. It is puzzling that in the Menard area extension is accommodated on the ridge flanks instead of within the transform fault. It is possible that the pattern of mantle upwelling around MTF provides a broad zone of magma source for the off-axis seamounts. We suggest that the offset zones of mantle upwelling and melt production might induce a thermal weakening of the lithosphere, allowing the deformation of the lithosphere south of the MTF following the change in spreading direction.

Flexural and membrane stresses induced in the lithosphere by the load of one volcano may explain the formation of some of the observed ridges [Hieronymus and Bercovici, 1999; Hieronymus and Bercovici, 2000; Shen, *et al.*, 1995]. In this process, a first volcano or chain of volcanoes is first generated, and the others, or the other chains and ridges, form due to the induced flexural stresses. The 42°S Ridges and the southern line in the South Menard area may result from this process. This mechanism may also explain the division of the North Menard volcanoes into distinct groups.

Summary and conclusions

Our analysis of the bathymetry, backscatter, gravity and geochemistry data of some large ridges near the Pacific-Antarctic ridge provides insight into the dynamics of mantle upwelling and lithospheric deformation in the area. The volcanic activity, as suggested by the young K/Ar ages of some samples and by the strong backscatter in sonar images, appears to be limited to areas of seafloor younger than about 3 Ma. The seamount chains show recent activity close to the ridge axis, and only the South Menard ridge is affected by extensional faulting. The off-axis volcanoes south of the Menard TF are aligned in two ridges, the northern one extending to seafloor aged 5 Ma, the southern one to 3 Ma. Both ridges show recent volcanic flows in the center of the ridges, and are affected by N-S extension. They consist of two different types of volcanoes: conical, flat-topped ones and rough, elongated ones associated to narrow, EW-trending volcanic ridges, some of them associated with strong acoustic backscatter on the EM12 imagery.

We have shown that the volcanic ridges on the flanks of the PAR likely tap the axial melting zone and anomalous melting zones in the mantle near the ridge axis, reflecting off-axis mantle upwelling. Such anomalies might result from three-dimensional mantle upwelling, offset from the ridge axis to the Pacific ridge flanks as a result of the change in spreading direction in the last 5 Ma. The ridges south of the Menard TF also result from tectonic deformation. We suggest that a recent clockwise change in the relative plate motion (near 5 Ma) might have increased the tensile stresses in the young lithosphere, easing the extraction of magma to the seafloor and allowing for the formation of the seamounts.

Acknowledgements :

We thank the Captain and crew of N/O L'Atalante for their great work in challenging weather conditions during the cruise. We also thank the scientific party of the

Pacantarctic2 cruise for their help in data acquisition and processing and their enthusiasm at sea. Thanks also to F. Martelozzo and W. Joseph-Louis for data processing. Many thanks to Eliane le Drezen for her help with the imagery processing. Some processing and all figures were done using GMT software [Wessel and Smith, 1991]. We are grateful to Milene Cormier, James Conder, and an anonymous reviewer for very thorough and constructive comments.

References:

- Barrat, J.-A., F. Keller, J. Amossé, R. N. Taylor, R. W. Nesbitt, and T. Hirata (1996), Determination of rare earth elements in sixteen silicate reference samples by ICP-MS after Tm addition and ion exchange separation, *Geostandards Newsletter*, 20, 133-139.
- Barrat, J.-A., A. Yamauchi, R. C. Greenwood, M. Bohn, J. Cotten, M. Benoit, and I. A. Franchi (2007), The Stannern trend eucrites: Contamination of main group eucritic by crustal partial melts, *Geochimica et Cosmochimica Acta*, 71, 4108-4124.
- Bell, R. E., and W. R. Buck (1992), Crustal control of ridge segmentation inferred from observations of the Reykjanes Ridge, *Nature*, 357, 583-586.
- Briais, A., D. Aslanian, L. Geli, and H. Ondreas (2002), Analysis of propagators along the Pacific-Antarctic Ridge: evidence for triggering by kinematic changes, *Earth Planet. Sci. Lett.*, 199, 415-428.
- Cande, S. C., C. A. Raymond, J. Stock, and W. F. Haxby (1995), Geophysics of the Pitman fracture zone and Pacific-Antarctic plate motions during the Cenozoic, *Science*, 270, 947-953.
- Cande, S. C., and J. M. Stock (2004), Pacific-Antarctic-Australia motion and the formation of the Macquarie Plate, *Geophys. J. Int.*, 157, 399-414.
- Cassignol, C., Y. Cornette, B. David, and P. Y. Gillot (1978), Technologie potassium-argon, C.E.N., Saclay, *Rapp. CEA R-4802*, 37 pp.
- Charbit, S., H. Guillou, and L. Turpin (1998), Cross calibration of K-Ar standard minerals using an unspiked Ar measurements technique, *Chem. Geol.*, 150, 147-159.
- Conder, J. A., D. W. Forsyth, and E. M. Parmentier (2002), Asthenospheric flow and asymmetry of the East Pacific Rise, MELT area, *J. Geophys. Res.*, 107, 2344, doi:2310.1029/2001JG000807.
- Croon, M. B., S. C. Cande, and J. M. Stock (2008), Revised Pacific-Antarctic plate motions and geophysics of the Menard Fracture Zone, *Geochem. Geophys. Geosyst.*, 9, doi: 10:1029/2008GC002019.
- Davis, E. E., and J. L. Karsten (1986), On the cause of the asymmetric distribution of seamounts about the Juan de Fuca ridge: ridge-crest migration over a heterogeneous asthenosphere, *Earth Planet. Sci. Lett.*, 79, 385-396.
- Dosso, L., et al. (2005), The Pacific-Antarctic Ridge between 41°15'S and 52°45'S: Survey and sampling during the PACANTARCTIC 2 cruise, *InterRidge News*, 14, 6.
- Dumoulin, C., M. P. Doin, D. Arcay, and L. Fleitout (2005), Onset of small-scale instabilities at the base of the lithosphere: scaling laws and role of pre-existing lithospheric structures, *Geophys. J. Int.*, 160, 344-356.
- Etoubleau, J., P. Cambon, H. Bougault, and J. L. Joron (1999), Precise quantitative determination of Niobium at low level concentrations in geological samples by WD-XRF, *Geostandards Newsletter*, 23, 187-195.

- Forsyth, D. W., N. Harmon, D. S. Scheirer, and R. A. Duncan (2006), Distribution of recent volcanism and the morphology of seamounts and ridges in the GLIMPSE study area: Implications for the lithospheric cracking hypothesis for the origin of intraplate, non-hot spot volcanic chains, *J. Geophys. Res.*, *111*, B11407, doi:10.1029/2005JB004075.
- Gans, K. D., D. S. Wilson, and K. C. Macdonald (2003), Pacific Plate gravity lineaments: Diffuse extension or thermal contraction?, *Geochem. Geophys. Geosyst.*, *4* (9), 1074, doi:10.1029/2002GC000465.
- Géli, L., et al. (1997), Evolution of the Pacific-Antarctic Ridge south of the Udintsev Fracture Zone, *Science*, *278*, 1281-1284.
- Gillot, P. Y., and Y. Cornette (1986), The Cassinot technique for K-Ar dating, precision and accuracy: examples from the late Pleistocene to recent volcanics from southern Italy, *Chem. Geol.*, *59*, 205-222.
- Gomez, O., and A. Briais (2000), Near-axis seamount distribution and its relationship with the segmentation of the East Pacific Rise and northern Pacific-Antarctic Ridge, 17°N-56°S, *Earth Planet. Sci. Lett.*, *175*, 233-246.
- Gripp, A. E., and R. G. Gordon (2002), Young tracks of hotspots and current plate velocities, *Geophys. J. Int.*, *150*, 321-361.
- Guillou, H., J. C. Carracedo, F. J. Perez Torrado, and E. Rodriguez Badiola (1996), K-Ar ages and magnetic stratigraphy of a hotspot-induced, fast-grown oceanic island: El Hierro, Canary Islands, *J. Volc. Geotherm. Res.*, *73*, 141-154.
- Harmon, N., D. W. Forsyth, and D. S. Scheirer (2006), Analysis of gravity and topography in the GLIMPSE study region: Isostatic compensation and uplift of the Sojourn and Hotu Matua Ridge systems, *J. Geophys. Res.*, *111*, B11406, doi:10.1029/2005JB004071.
- Haxby, W. F., and J. K. Weissel (1986), Evidence for small-scale mantle convection from Seasat altimeter data, *J. Geophys. Res.*, *91*, 3507-3520.
- Hieronymus, C. F., and D. Bercovici (1999), Discrete alternating hotspot islands formed by interaction of magma transport and lithospheric flexure, *Nature*, *397*, 604-607.
- Hieronymus, C. F., and D. Bercovici (2000), Non-hotspot formation of volcanic chains: control of tectonic and flexural stresses on magma transport, *Earth Planet. Sci. Lett.*, *181*, 539-554.
- Kincaid, C., D. W. Sparks, and R. Detrick (1996), The relative importance of plate-driven and buoyancy-driven flow at mid-ocean ridges, *J. Geophys. Res.*, *101*, 16,177-116,193.
- Kleinrock, M. C., and R. N. Hey (1989), Detailed tectonics near the tip of the Galapagos 95.5°W propagator: How the lithosphere tears and a spreading axis develops, *J. Geophys. Res.*, *94*, 13,801-813,838.
- Klingelhofer, F., H. Ondreas, A. Briais, C. Hamelin, and L. Dosso (2006), New structural and geochemical observations from the Pacific-Antarctic Ridge between 52°45'S and 41°15'S, *Geophys. Res. Lett.*, *33*, L21312, doi:10.1029/2006GL027335.
- Lonsdale, P. (1986), Tectonic and magmatic ridges in the Eltanin Fault System, South Pacific, *Mar. Geophys. Res.*, *8*, 203-242.
- Lonsdale, P. (1994), Geomorphology and structural segmentation of the crest of the southern (Pacific-Antarctic) East Pacific Rise, *J. Geophys. Res.*, *99*, 4683-4702.
- Lynch, M. A. (1999), Linear ridge groups: Evidence for tensional cracking in the Pacific Plate, *J. Geophys. Res.*, *104*, 29321-29333.

- Maia, M., et al. (2000), The Pacific-Antarctic Ridge-Foundation hotspot interaction : a case study of a ridge approaching a hot spot, *Mar. Geol.*, *167*, 61-84.
- Maia, M., C. Hémond, and P. Gente (2001), Contrasted interactions between plume, upper mantle, and lithosphere: Foundation chain case, *Geochem. Geophys. Geosyst.*, *2*, doi:10.1029/2000GC000117.
- Mayes, C. L., L. A. Lawver, and D. T. Sandwell (1990), Tectonic history and new isochron chart of the South Pacific, *J. Geophys. Res.*, *95*, 8543-8567.
- MELT Seismic Team (1998), Imaging the deep seismic structure beneath a mid-ocean ridge: the MELT experiment, *Science*, *280*, 1215-1218.
- Molnar, P., T. Atwater, J. Mammerickx, and S. M. Smith (1975), Magnetic anomalies, bathymetry and the tectonic evolution of the South Pacific since the Late Cretaceous, *Geophys. J. R. astr. Soc.*, *40*, 383-420.
- Müller, R. D., W. R. Roest, J.-Y. Royer, L. M. Gahagan, and J. G. Sclater (1997), Digital isochrons of the world's ocean floor, *J. Geophys. Res.*, *102*, 3211-3214.
- Ondréas, H., D. Aslanian, L. Géli, J. L. Olivet, and A. Briais (2001), Variations in axial morphology, segmentation, and seafloor roughness along the Pacific-Antarctic Ridge between 56°S and 66°S, *J. Geophys. Res.*, *106*, 8521-8546.
- Parker, R. L. (1972), The rapid calculation of potential anomalies, *Geophys. J. R. Astron. Soc.*, *31*, 447-455.
- Phipps Morgan, J., W. J. Morgan, Y.-S. Zhang, and W. H. F. Smith (1995), Observational hints for a plume-fed, suboceanic asthenosphere and its role in mantle convection, *J. Geophys. Res.*, *100*, 12753-12767.
- Pockalny, R. A., P. J. Fox, D. J. Fornari, K. C. Macdonald, and M. R. Perfit (1997), Tectonic reconstruction of the Clipperton and Siqueiros Fracture Zones: Evidence and consequences of plate motion changes for the last 3 Myr, *J. Geophys. Res.*, *102*, 3167-3181.
- Rabinowicz, M., and A. Briais (2002), Temporal variations of the segmentation of slow to intermediate-spreading mid-ocean ridges: 2. A 3-D model in terms of lithosphere accretion and convection within the partially molten mantle beneath the ridge axis, *J. Geophys. Res.*, *107*(B6), doi:10.1029/2001JB000343.
- Rabinowicz, M., S. Rouzo, J.-C. Sempéré, and C. Rosemberg (1993), Three-dimensional mantle flow beneath mid-ocean ridges, *J. Geophys. Res.*, *98*, 7851-7869.
- Ravilly, M., H. Horen, M. Perrin, J. Dyment, P. Gente, and H. Guillou (2001), NRM intensity of altered oceanic basalts across the MAR (21°N, 0–1.5 Myr): A record of geomagnetic paleointensity variations, *Geophys. J. Int.*, *145*, 401-422.
- Rusby, R., and R. C. Searle (1995), A history of the Easter microplate: 5.25 Ma to Present, *J. Geophys. Res.*, *100*, 12617-12640.
- Sandwell, D., and Y. Fialko (2004), Warping and cracking of the Pacific plate by thermal contraction, *J. Geophys. Res.*, *109*, 1-12.
- Sandwell, D. T., and W. H. F. Smith (1997), Marine gravity anomaly from Geosat and ERS1 satellite altimetry, *J. Geophys. Res.*, *102*, 10,039-10,054.
- Sandwell, D. T., and W. H. F. Smith (2005), Retracking ERS-1 altimeter waveforms for optimal gravity field recovery, *Geophys. J. Int.*, *163*, 79-89.
- Scheirer, D. S., and K. C. Macdonald (1995), Near-axis seamounts on the flanks of the East Pacific Rise, 8°N to 17°N, *J. Geophys. Res.*, *100*, 2239-2259.
- Scheirer, D. S., K. C. Macdonald, D. W. Forsyth, and Y. Shen (1996), Abundant

- seamounts of the Rano Rahi Seamount Field near the Southern East Pacific Rise, 15°S to 19°S, *Mar. Geophys. Res.*, *18*, 13-52.
- Searle, R. C. (1983), Multiple, closely-spaced transform faults in fast-slipping fracture zones, *Geology*, *11*, 607-610.
- Searle, R. C., J. Francheteau, and R. Armijo (2006), Compressional deformation north of the Easter microplate: a manned submersible and seafloor gravity investigation, *Geophys. J. Int.*, *164*, 359-369.
- Shen, Y., D. W. Forsyth, D. Scheirer, and K. C. Macdonald (1993), Two forms of volcanism; implications for mantle flow and off-axis crustal production on the west flank of the Southern East Pacific Rise, *J. Geophys. Res.*, *98*, 17875-17889.
- Shen, Y., D. S. Scheirer, D. W. Forsyth, and K. C. Macdonald (1995), Trade-off in production between adjacent seamount chains near the East Pacific Rise, *Nature*, *373*, 140-143.
- Smith, D. K., and T. H. Jordan (1987), The size distribution of Pacific seamounts, *Geophys. Res. Lett.*, *14*, 1119-1122.
- Smith, W. H. F., and D. T. Sandwell (1997), Global sea floor topography from satellite altimetry and ship depth soundings, *Science*, *277*, 1956-1962.
- Steiger, R. H., and E. Jäger (1977), Subcommittee on the geochronology: Convention on the use of decay constants in geo- and cosmochronology, *Earth Planet. Sci. Lett.*, *36*, 359-362.
- Stein, C. A., and S. Stein (1992), A model for the global variation in oceanic depth and heat flow with lithospheric age, *Nature*, *359*, 123-129.
- Toomey, D. R., D. Joussetin, R. A. Dunn, W. S. D. Wilcock, and R. S. Detrick (2007), Skew of mantle upwelling beneath the East Pacific Rise governs segmentation, *Nature*, *446*, 409-414, doi:410.1038/nature05679.
- van Hunen, J., and S. Zhong (2006), Influence of rheology on realignment of mantle convective structure with plate motion after a plate reorganization, *Geochem. Geophys. Geosyst.*, *7*, 1-14.
- Vlastelic, I., L. Dosso, H. Guillou, H. Bougault, L. Géli, J. Etoubleau, and J. L. Joron (1998), Geochemistry of the Hollister Ridge: relation with the Louisville hotspot and the Pacific-Antarctic Ridge, *Earth Planet. Sci. Lett.*, *160*, 777-793.
- Vogt, P. R. (1974), Volcano height and plate thickness, *Earth Planet. Sci. Lett.*, *23*, 337-348.
- Weeraratne, D. S., D. W. Forsyth, Y. Yang, and S. C. Webb (2007), Rayleigh wave tomography beneath intraplate volcanic ridges in the South Pacific, *J. Geophys. Res.*, *112*, B06303, doi:06310.01029/02006JB004403.
- Wessel, P., and L. Kroenke (2007), Reconciling late Neogene Pacific absolute and relative plate motion changes, *Geochem. Geophys. Geosyst.*, *8*, Q08001, doi:08010.01029/02007GC001636.
- Wessel, P., and S. Lyons (1997), Distribution of large Pacific seamounts from Geosat/ERS-1: implications for the history of intraplate volcanism, *J. Geophys. Res.*, *102*, 22,459-422,475.
- Wessel, P., and W. H. F. Smith (1991), Free Software Helps Map and Display Data, *Eos Trans. AGU*, *72*, 441.
- White, S. M., K. C. Macdonald, D. S. Scheirer, and M.-H. Cormier (1998), Distribution of isolated volcanoes on the flanks of the East Pacific Rise, 15.3°S-20°S, *J. Geophys. Res.*,

103, 30371-30384.

- White, S. M., K. C. Macdonald, and J. M. Sinton (2002), Volcanic mound fields on the East Pacific Rise, 16-19°S: Low effusion rate eruptions at overlapping spreading centers for the past 1 Myr, *J. Geophys. Res.*, 107, doi:10.1029/2001JB000483.
- Wilson, D. S. (1992), Focused mantle upwelling beneath mid-ocean ridges: evidence from seamount formation and isostatic compensation of topography, *Earth Planet. Sci. Let.*, 113, 41-55.
- Yelles-Chaouche, K., J. Francheteau, and P. Patriat (1987), Evolution of the Juan-Fernandez microplate during the last 3 million years, *Earth Planet. Sci. Let.*, 86, 253-268.

Figure captions

Figure 1: Shaded map of the free-air gravity anomaly derived from satellite altimetry [Sandwell and Smith, 1997; Sandwell and Smith, 2005]. White frame is location of Figure 2. Red dots are earthquake epicenters (1976 to 2007) from Harvard CMT. Black line is ship track for Pacantarctic2 cruise. Yellow arrows point to traces of propagators discussed in text. Top left inset : location of study area along Pacific-Antarctic ridge. Bottom right inset : focal mechanisms near Menard transform fault.

Figure 2: Shaded multibeam bathymetry combined with bathymetry predicted from altimetry. Thin white lines are isochrons every 2 Ma [Müller *et al.*, 1997]. In red are the segment boundaries and names defined in Klingelhoefer *et al.* [2006].

Figure 3: a: Backscatter imagery of the volcanic constructions near 42°S. Dark is high backscatter. b: Shaded multibeam bathymetry in same area as a, and color contoured bathymetry predicted from satellite altimetry [Smith and Sandwell, 1997]. Black dots and labels mark dredge locations and numbers. Red numbers are K/Ar ages. Rose diagram shows distribution of the fault scarp orientations, weighed by length and binned every 10°. Blue arrow is absolute Pacific plate motion. Dotted lines are flow lines or relative plate motion, estimated from Euler poles of rotation of Cande and Stock (2004). Grey lines are isochrones every Ma. Bold black line is ridge axis. Solid black lines are major scarps, corresponding to closely-spaced, straight bathymetric contours on bathymetry maps, or high backscatter, straight, continuous lines on imagery. Grey dashed box is area of volume calculation (see text).

c: Backscatter imagery of the Gros Temps volcanic ridge. d: Shaded multibeam bathymetry of same area as 3c. Same legend and color scales as Figures 3a and b.

e: Backscatter imagery of the North Menard volcanic ridge. f: Shaded multibeam bathymetry of same area as 3e. Same legend as Figure 3b.

g: Backscatter imagery of the South Menard volcanic ridges. h: Shaded multibeam bathymetry of same area as 3g. Same legend as Figure 3b, except that blue arrows show absolute Antarctic plate motion.

Figure 4: Volume of the surveyed volcanic ridges as a function of crustal age (ages from Müller, *et al.*, 1997).

Figure 5: Residual mantle Bouguer anomalies (RMBA). Dotted lines delineate volcanic constructions .a,c) Residuals with respect to a model of constant crustal thickness with Moho parallel to bathymetry. b,d) Residuals with respect to a model of constant crustal thickness with smoothed Moho and lower volcano density.

Figure 6: Band-passed filtered gravity anomalies (wavelengths 80 to 600 km) derived from satellite gravity [Sandwell and Smith, 1997]. Black areas are maximum of the short wavelength anomalies, marking the seamounts, obtained by clipping the filtered gravity at 10 mGal.

Table 1: Comparison of volcanic ridge characteristics.

Table 2: Location and trace element concentrations of Pacantarctic2 off-axis samples.

Table 3: K-Ar ages of the Pacantarctic 2 samples. Decay constants used for the calculations are from [*Steiger and Jäger, 1977*].

Table 1. Comparison of volcanic ridge characteristics.

	42°S Ridges	Gros Temps	North Menard	South Menard	Rano Rahi (Scheirer et al., 1996)	Thanksgiving (Forsyth et al., 2006)
Start from the axis (km)	50–100	15	10	40	20	
Ridge length (km)	150–200	50	200	200	25 – >240	140
Ridge width (km)	5–10	10–15	10–15	10–20	~2–5	10
Volcano Diameters (km)	5–10	4–10	6	12	~2–5	10
Volcano Heights (m)	1500	1900	1000–190	1500–2000	200–1200	150
Volcano ages (Ma)	0.46 /2.16	no data	0.15/1.21	0.41/2.03		
Crustal ages (Ma)	2 – 6	0 – 2	0 – 5	1 – 5	0–6.5	
Volcano shape	Elongated ridge	coalescent	coalescent but linked by ridges	round-shape or robust	Isolated or linked by ridge	coalescent
Dredge result (this survey)	fresh pillows, pillows, and vacuolar basalts	no data	altered basalts and pillows	plagioclase-bearing pillows, aphyric fresh and altered pillows		

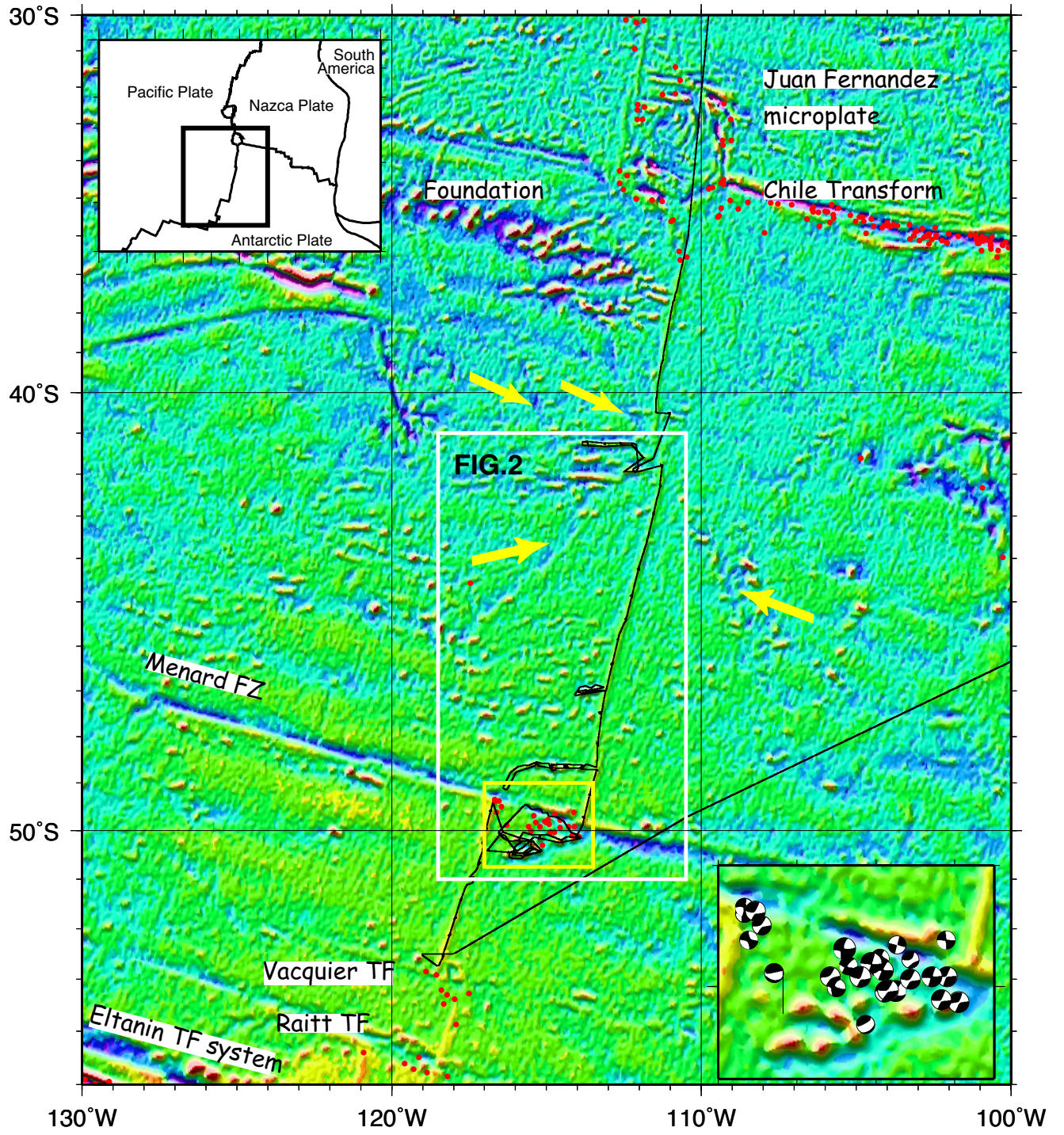
Table 2. Location and trace element concentrations of Pacant2 off-axis samples.

Sample	Latitude °S	Longitude °W	Nb	Zr	(Nb/Zr)_N
DR11-1	50.065	116.471	3.14	84	0.41
DR11-6			3.33	83	0.44
DR12-1	50.425	116.033	5.08	41	1.37
DR13-1	50.498	115.653	17.29	129	1.48
DR14-02	50.442	115.218	4.51	103	0.48
DR15-1	50.220	115.512	5.99	110	0.60
DR16-1g	50.197	115.891	3.31	70	0.52
DR16-6			3.40	71	0.53
DR16-7			3.18	69	0.51
DR17-1	50.149	115.261	4.01	90	0.49
DR18-4	50.236	114.495	4.06	76	0.59
DR19-2	50.142	113.975	5.74	83	0.76
DR19-3			4.75	110	0.48
DR23-1	48.667	113.818	86.5	391	2.44
DR23-2			86.6	389	2.46
DR24-1	48.644	114.370	3.23	98	0.36
DR24-3			2.92	93	0.35
DR25-2	48.609	114.786	3.99	99	0.44
DR26-1	48.614	115.260	1.67	73	0.25
DR39-04	41.253	113.685	1.21	64	0.21
DR42-1A	41.928	112.162	0.46	43	0.12
DR42-3			1.31	54	0.27
DR43-02	41.534	111.033	0.84	51	0.18

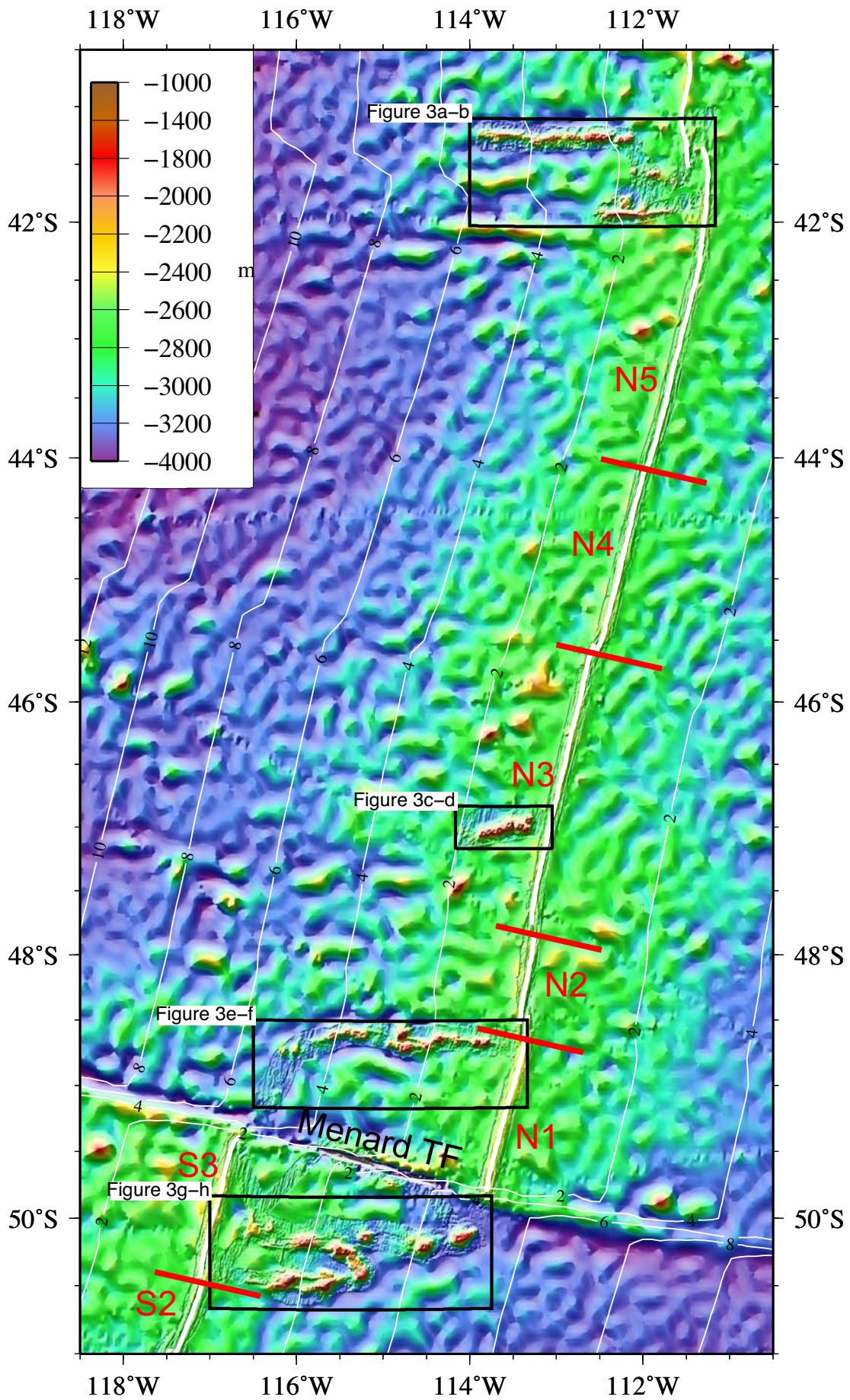
Table 3: K-Ar ages of the Pacantartic 2 samples. Decay constants used for the calculations are from Steiger and Jäger (1977).

Sample ID Experience #	Weight molten (g)	K* (wt.%)	$^{40}\text{Ar}^*$ (%)	$^{40}\text{Ar}^*$ (10^{-13} mol/g)	$^{40}\text{Ar}^*$ weighted mean $\pm 1\sigma$	Age $\pm 2\sigma$ (ka)
DR23-02						
7229	1.09359	1.644 ± 0.016	2.822	4.454		
7241	1.33235	1.644 ± 0.016	1.888	4.286	4.347 ± 0.073	152 ± 6
DR11-01						
7061	0.94956	0.187 ± 0.002	0.764	1.310		
7077	1.87010	0.187 ± 0.002	1.109	1.368	1.350 ± 0.063	416 ± 40
DR42-3						
7243	1.18313	0.083 ± 0.001	0.709	0.634		
7259	2.24981	0.083 ± 0.001	0.883	0.673	0.666 ± 0.428	463 ± 60
DR13-01						
7079	1.10451	0.461 ± 0.005	4.465	5.588		
7087	2.25019	0.461 ± 0.005	4.400	5.644	5.631 ± 0.054	704 ± 20
Sample ID Experience #	Weight molten (g)	K* (wt.%)	$^{40}\text{Ar}^*$ (%)	$^{40}\text{Ar}^*$ (10^{-13} mol/g)	$^{40}\text{Ar}^*$ weighted mean $\pm 1\sigma$	Age $\pm 2\sigma$ Ma
DR15-01						
7064	1.02807	0.227 ± 0.003	3.848	4.042		
7080	2.03216	0.227 ± 0.003	4.910	4.126	4.106 ± 0.053	1.04 ± 0.03
DR26-1						
7230	1.14762	0.050 ± 0.001	0.812	0.991		
7242	2.16833	0.050 ± 0.001	0.879	1.067	1.051 ± 0.048	1.21 ± 0.12
DR17-1						
7234	1.11446	0.266 ± 0.003	3.101	6.711		
7252	1.19334	0.266 ± 0.003	3.125	6.823	6.758 ± 0.068	1.46 ± 0.04
DR18-04						
7065	1.07152	0.188 ± 0.002	3.325	6.735		
7097	1.09002	0.188 ± 0.002	3.664	6.481	6.625 ± 0.081	2.03 ± 0.06
DR39						
7235	1.15879	0.224 ± 0.002	3.053	8.624		
7253	1.14790	0.224 ± 0.002	2.424	8.079	8.380 ± 0.079	2.16 ± 0.06

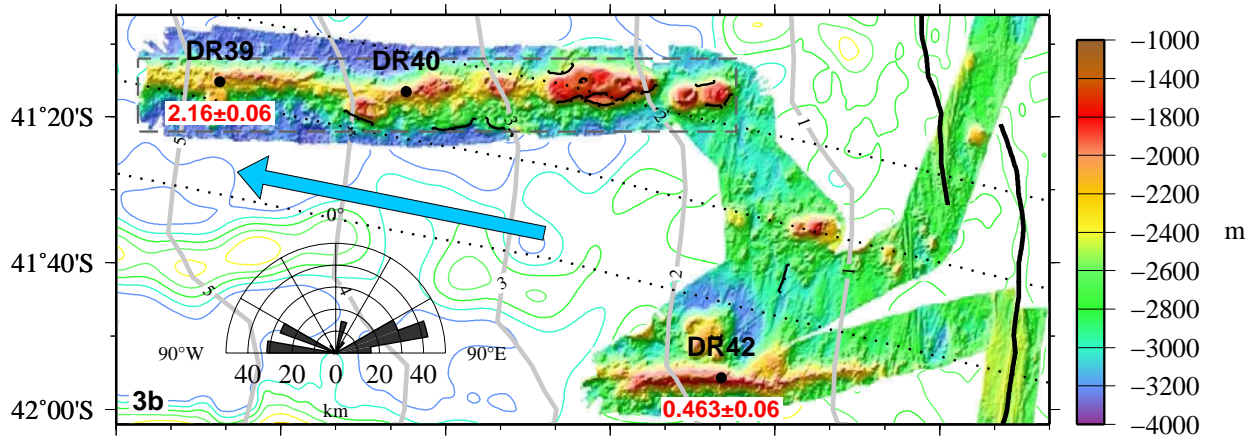
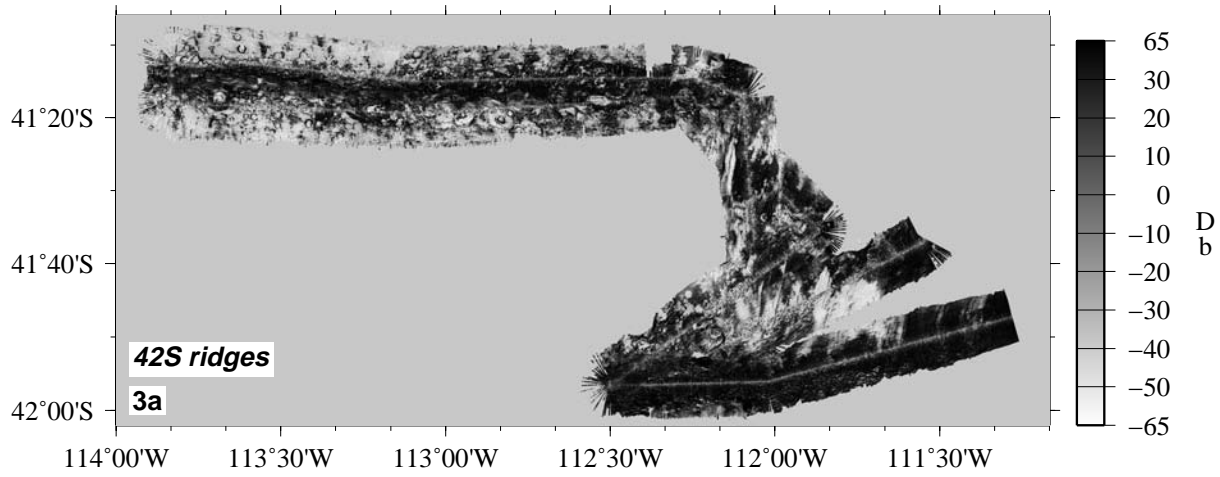
Briais et al. Figure 1



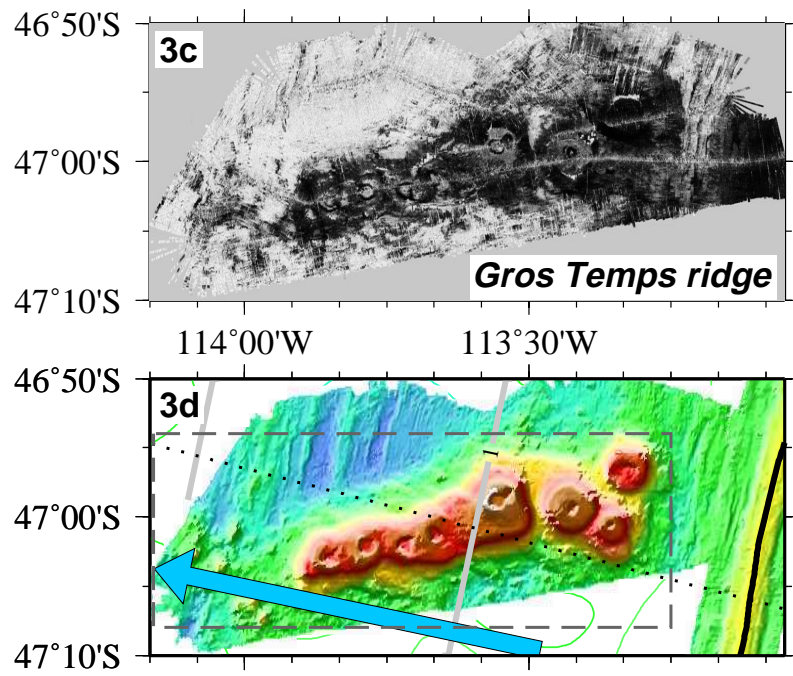
Briais et al. Figure 2



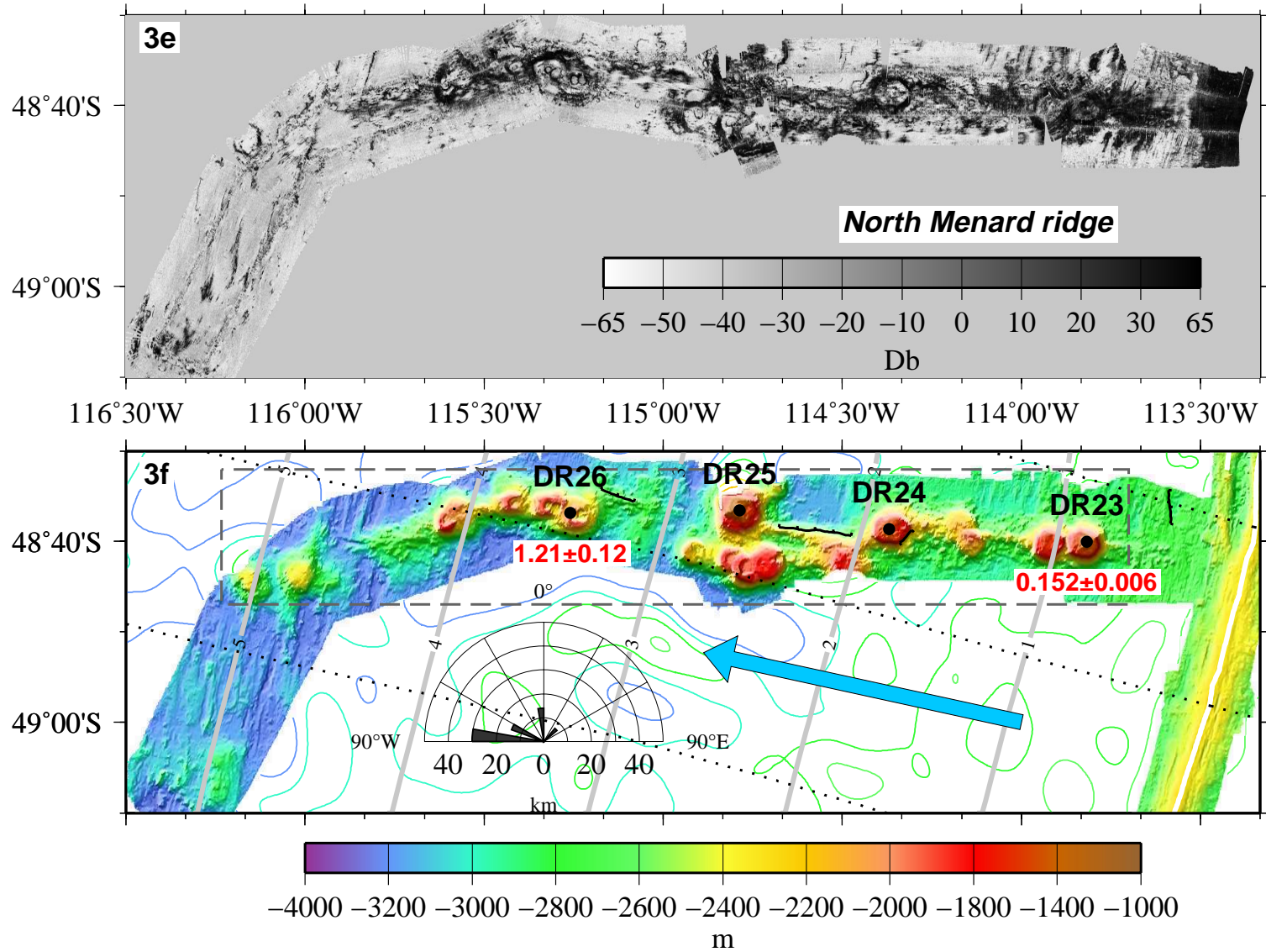
Brais et al. Figure 3a & 3b

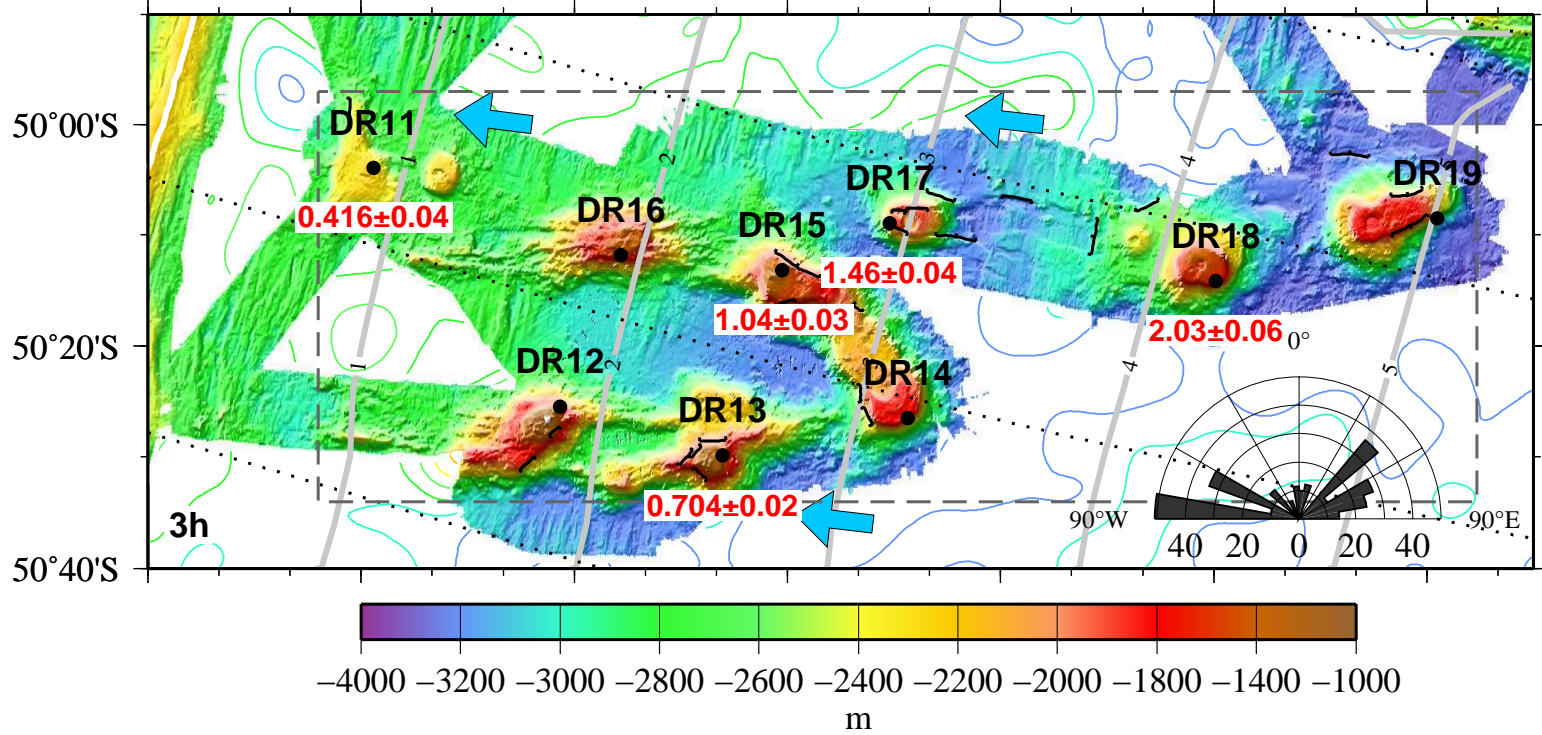
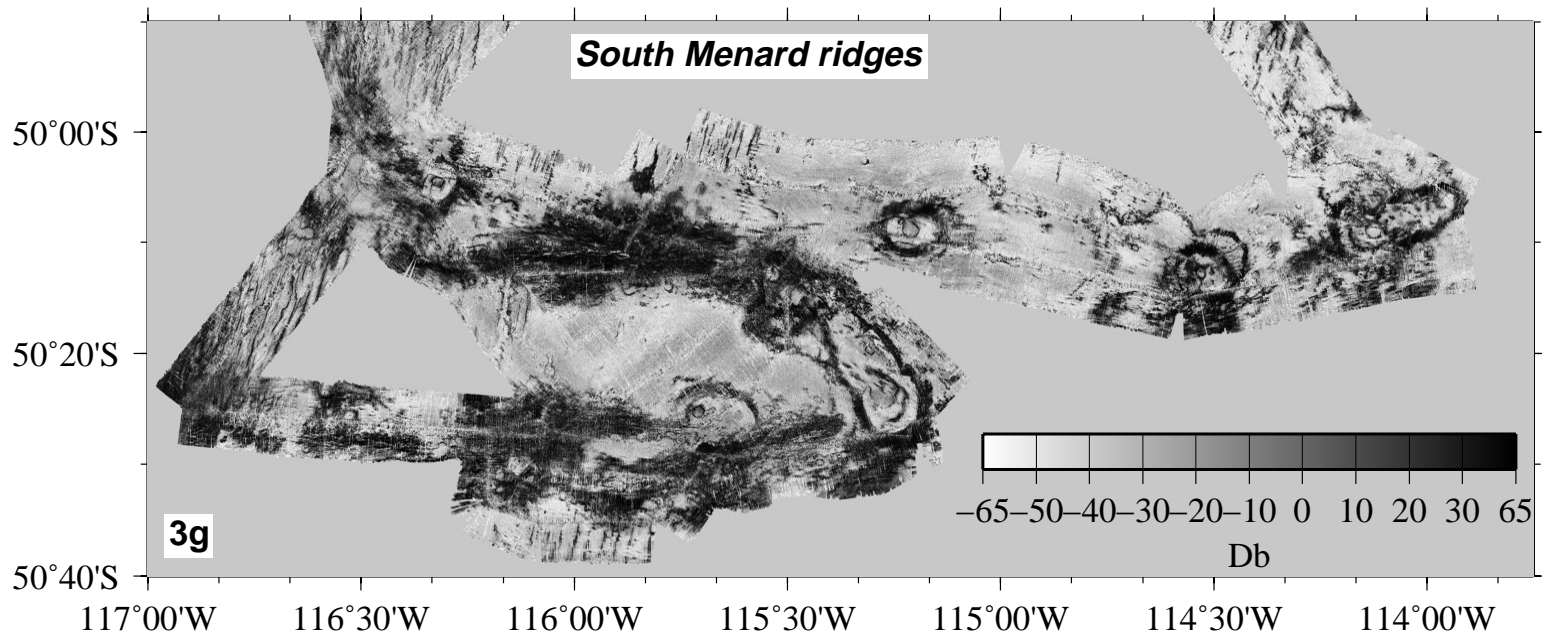


Briais et al. Figure 3c & 3d

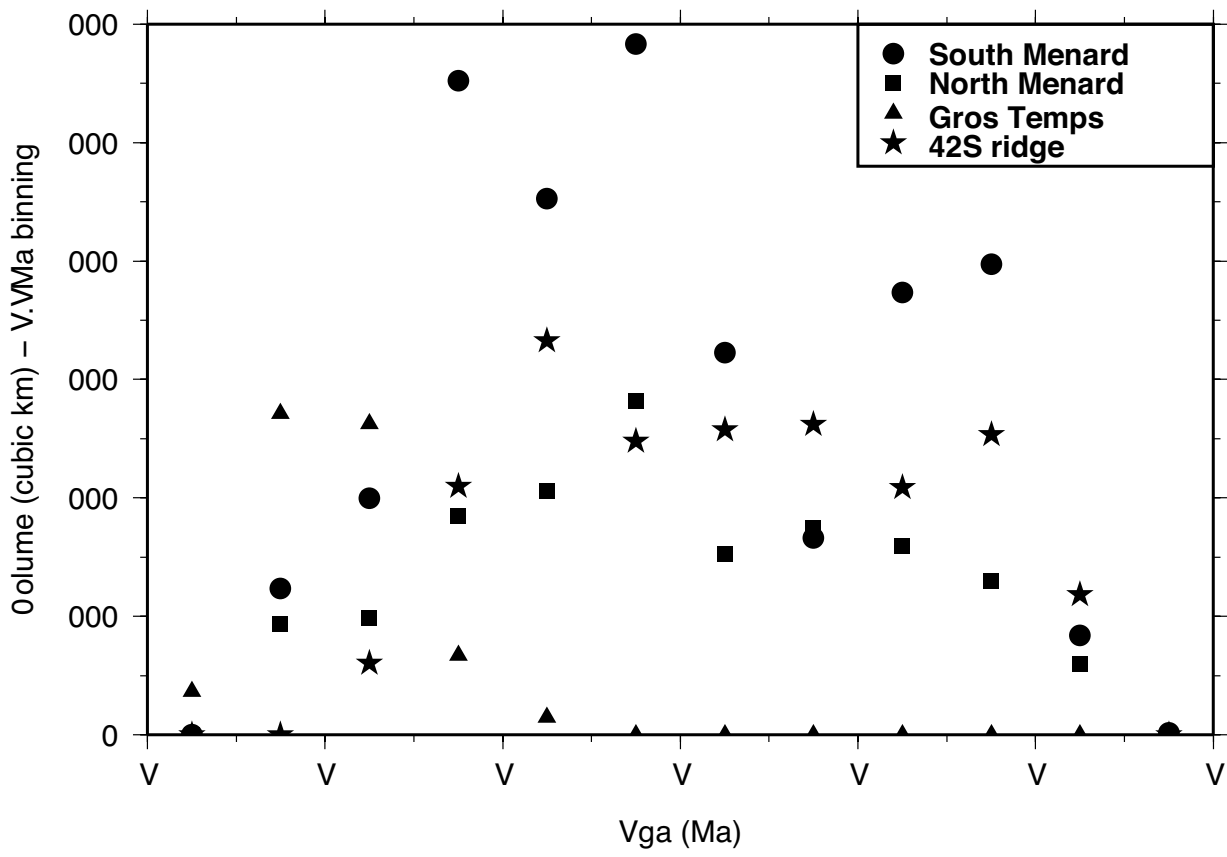


Briais et al. Figure 3e & 3f

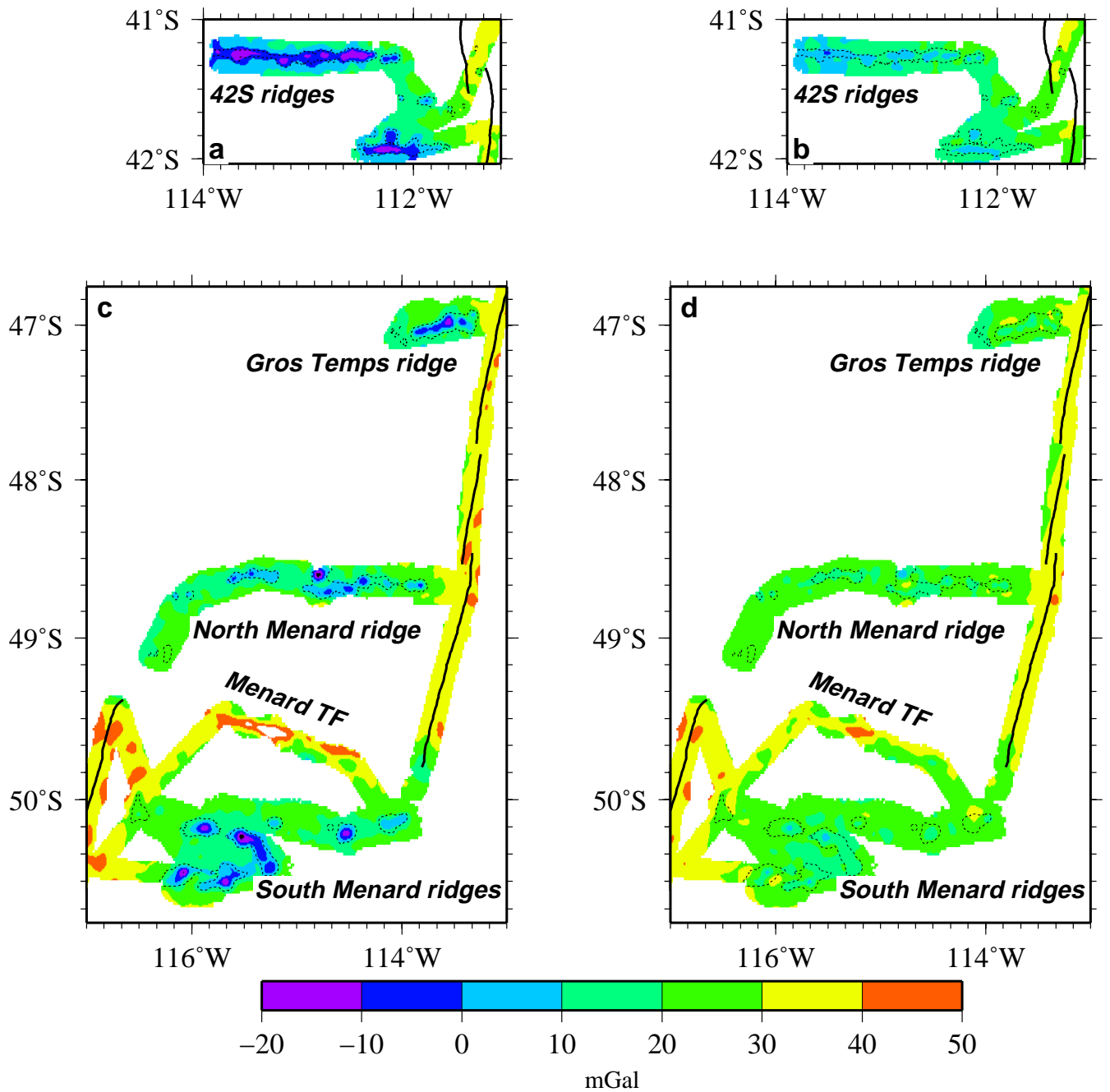




Vriaia at a.. Figura V



Briais et al. Figure 5



Briais et al. Figure 6

